Supplementary Material: The efficiency, timeliness, and permanence of CDR pathways: a comparative analysis

Solene Chiquier[a,b], Piera Patrizio[a,b], Mai Bui[a,b], Nixon Sunny[a,b] and Niall Mac Dowell[a,b]

[a]*Centre for Environmental Policy, Imperial College London, UK*
[b]*Centre for Process Systems Engineering, Imperial College London, UK*

SM. Supplementary materials

SM.1. Energy & GHG data

We assume the decarbonisation of the energy sector by the end of the century as follows.

SM.1.1. Fuels

Current (fossil) fuels are replaced gradually by bio-fuels between 2040 and 2080, as shown in **Eq. A.1**:

$$CI_{fuel}(t) = \%_{fossil\,fuel}(t) \times CI_{fossil\,fuel}(2020) + \%_{bio-fuel}(t) \times CI_{bio-fuel}(2020) \quad (Eq.\ A.1)$$

where: $CI_{fuel}(t)$ is the carbon intensity of fuels over time (kg CO_{2eq}/l), and t is time (yrs). $CI_{fossil\,fuel}(2020)$ and $CI_{bio-fuel}(2020)$ are the current carbon intensities (direct and indirect emissions) of fossil-fuels and bio-fuels (kg CO_{2eq}/l), respectively, as shown in **Table A.1**, and $\%_{fossil\,fuel}(t)$ and $\%_{bio-fuel}(t)$ are the shares of fossil fuels and bio-fuels over time (%), respectively. Also, $\%_{fossil\,fuel}(t) + \%_{bio-fuel}(t) = 1$.

Table A.1 (Current) direct and indirect carbon intensities for fuels.

Type of fuel	Direct emissions (kg CO_{2eq}/l)	Indirect emissions (kg CO_{2eq}/l)
diesel	2.55	0.61
bio-diesel	0.17	0.37

SM.1.2. Electricity

Electricity becomes carbon-neutral by 2050, using (region-specific) projections of the IPCC illustrative pathway P2[1], as shown in **Eq. A.2**:

$$CI_{elec}(t) = CI_{elec}(2020) \times \%_{decarbonisation}(t) \quad (Eq.\ A.2)$$

where: $CI_{elec}(t)$ is the carbon intensity of electricity over time (g CO_{2eq}/kWh), and t is time (yrs). $CI_{elec}(2020)$ is the current carbon intensity of electricity (g CO_{2eq}/kWh), as shown in **Table A.2**, and $\%_{decarbonisation}(t)$ is the decarbonisation share over time (%).

Table A.2 (Current) electricity carbon intensities in different regions.

Region	Indirect emissions	Indirect emissions

	(g $CO2_{eq}$/kWh)	(g $CO2_{eq}$/MJ)
Brazil	130	36
China	735	204
UK	313	87
India	854	237
USA	470	131

The net-zero transition of the electricity grid in different regions is illustrated in **Fig. A.1**. For example, India has the highest electricity carbon intensity in 2020 (*i.e.,* 854 g CO_{2eq}/kWh) and Brazil has the lowest one (*i.e.,* 130 g CO_{2eq}/kWh), whereas electricity carbon intensities reach toward net-zero in all

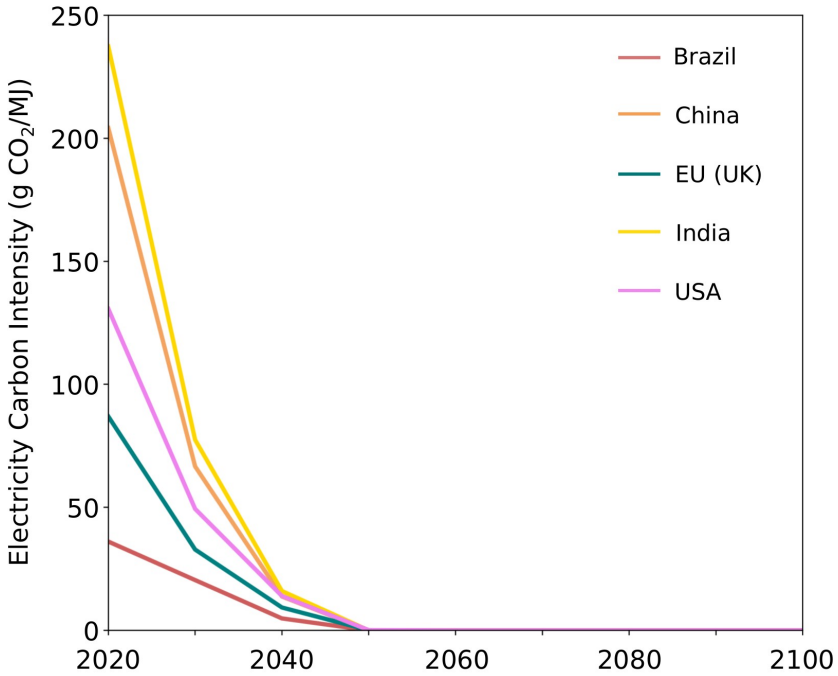

Fig. A.1 Decarbonisation of the electricity mix, following the IPCC P2 illustrative pathway.

regions by 2050.

SM.1.3. Natural Gas & Hydrogen

Thermal energy is required for sorbent regeneration in the case of liquid solvent DACCS. Because the regeneration temperature is around 900°C[2,3], only natural gas has been suggested to supply such high-grade heat. However, it is still unclear what the decarbonisation trend of natural gas will be. In this study, we also consider hydrogen (H_2) for the supply of high-grade heat, for which a decarbonation trend is clearer and more likely. Current and near-future H_2 is therefore assumed to be produced *via* natural gas steam methane reforming (SMR), which is currently highly carbon intensive (the current indirect carbon intensity for SMR-based H_2 is 9.1 times higher than for natural gas), and then to transition progressively between 2040 and 2080 to green H_2 (*i.e.,* produced from electrolysis). As green H_2 will be produced with grid electricity, which is subject to decarbonisation and will become net zero by 2050, green hydrogen will become net-zero by 2050 as well. This is shown in **Eq. A.3-4**:

$$CI_{H_2}(t) = \%_{SMR-H_2}(t) \times CI_{SMR-H_2}(2020) + \%_{elec}(t) \times CI_{elec-H_2}(t)$$

$$(Eq.\ A.3)$$

$$CI_{elec-H_2}(t) = CI_{elec-H_2}(2020) \times \%_{decarbonisation}(t)$$
$$(Eq.\ A.4)$$

where: $CI_{H_2}(t)$ is the carbon intensity of H_2 over time (g CO_{2eq}/MJ), and t is time (yrs). $CI_{SMR-H_2}(2020)$ and $CI_{elec-H_2}(2020)$ are the current carbon intensities (indirect emissions only) of SMR-based and green H_2 (g CO_{2eq}/MJ), respectively, and $CI_{elec-H_2}(t)$ is the carbon intensity of green H_2 over time (g CO_{2eq}/MJ), as shown in **Table A.3**. $\%_{SMR-H_2}(t)$ and $\%_{elec-H_2}(t)$ are the shares of SMR-based and green H_2 over time (%), receptively. Also, $\%_{SMR-H_2}(t) + \%_{elec-H_2}(t) = 1$.

Table A.3 Current and projected carbon intensities for natural gas and hydrogen (H_2).

Type of fuel	Direct emissions (g CO_{2eq}/MJ)	Indirect emissions (g CO_{2eq}/MJ)
Natural gas†	56.59	11.74
Currently steam-reforming H_2	0	109.4
Currently electrolysis H_2	0	175.0
Zero-carbon electrolysis H_2	0	0

† The direct CO_2 emissions from the combustion of natural gas are 100% captured within the liquid solvent DACCS process, and are therefore not accounted for in DACCS CDR efficiency.

SM.2. Afforestation/Reforestation (AR)

This section presents the main assumptions that have been adopted for parameterizing AR in the MONET framework.

SM.2.1. Value Chain & Sankeys

In this study, AR is explicitly spatio-temporally modelled into 5 integrated sub-models[4]: 1) a forest growth model, 2) a forest management cycle model, 3) a biogenic carbon (and CO_2) sequestration

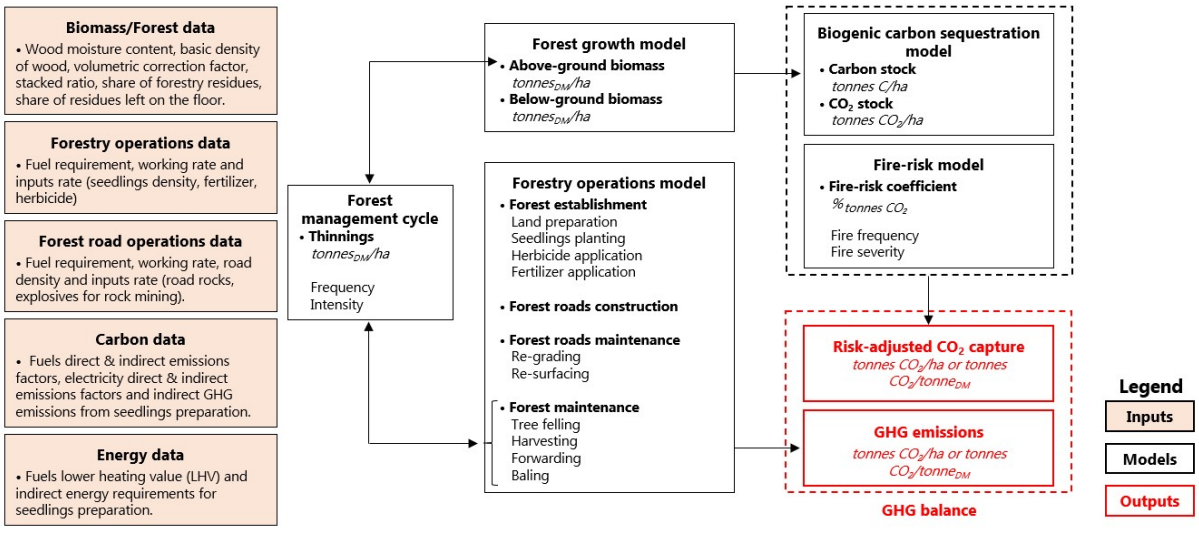

Fig. A.2 Schematic of the AR's whole-system model, outlining the interactions between 5 integrated sub-models: 1) a forest growth model, 2) a forest management cycle model, 3) a biogenic carbon (and CO_2 sequestration model, and 4) its associated "fire-penalty" model, and 5) a forestry operations model.

model and 4) its associated "fire-penalty" model, and 5) a forestry operations model. This is shown in **Fig. A.2** :

Within the forest growth model, forest growth curves are characterised by ecological zone and forest type (broadleaves/conifers), to account for geographic, climatic and ecological variations[5]. Both the above-ground biomass—the vegetation above the soil, such as stems, branches, foliage or bark—and the below-ground biomass—the roots—are included in the forest growth model. For example, temperate oceanic forests dominate the ecology of the UK—88% of the land cover in the UK[5]—and conifers and broadleaves account for around half of the UK forest area—49% and 51% respectively[6]. By using this ecological zone and this distribution of tree species as a proxy for the UK, the maximum CO_2 sequestration potential of forests in the UK is 398 tCO_2/ha (327 and 71 t CO_2/ha in above-ground and below-ground biomass, respectively).

Within the forest management cycle model, forest stands are subject to a non-intensive forest management—with reduced or minimum human intervention. The purpose of this forest management is to maximise and maintain the carbon (and CO_2) sequestration potential of the forest (calculated in the biogenic carbon sequestration model) by clearing the forest of old and/or sick trees in order to let younger trees grow, more vigorously and with more space. In particular, the forest management cycle model directly determines the proportion of above-ground biomass that needs to be thinned for the aforementioned reasons. Indirectly, it also impacts the proportion of below-ground biomass that remains after. Fig. A.3 shows the forest growth, as calculated here, for different regions and climates, subject to forest management.

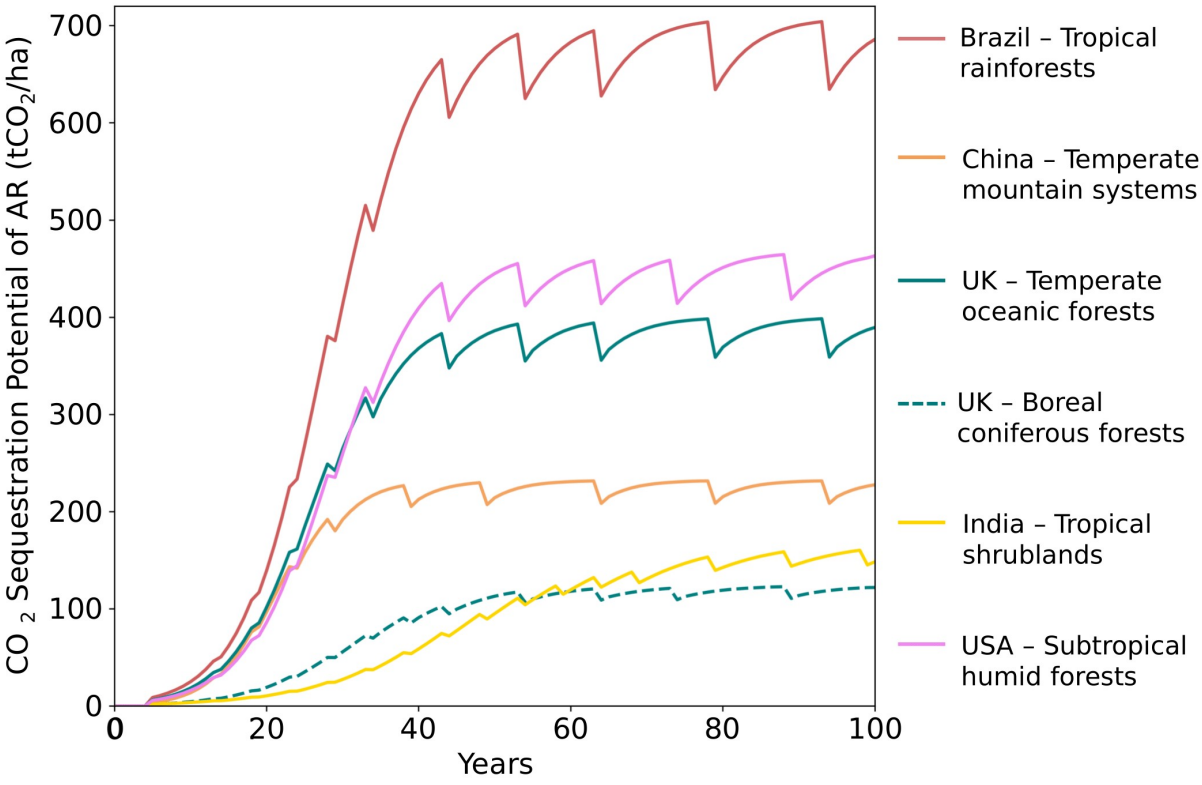

Fig. A.3 Evolution of the CO_2 sequestration potential of AR for different climates and regions, subject to forest management activities. AR has the highest CDR potential in warm and humid climates, *e.g.*

Brazil (tropical rainforests) here, and the lowest in cold and/or dry climates, *e.g.* UK (boreal coniferous forests) or India (tropical shrublands).

Finally, the "fire-risk" model evaluates the risk of wildfires over time, that discount the CO_2 sequestration of AR. This is described in Section A.2.2 below.

Within the forestry operation model, a set of forestry operations—forest establishment and management—is defined and evaluated in term of their energy requirements and associated CO_2 emissions[7–9]. These include forest establishment, forest roads construction and maintenance, and forest maintenance. Specifically, CO_2 (and N_2O) emissions are accounted for, at each step of the forestry operations model.

Overall, the CO_2 removal efficiency of AR $CO_2\ removal\ efficiency^{AR}(t)$ (%) is calculated as follows (**Eq. A.5-6**):

$$CO_2\ removal\ efficiency^{AR}(t) = \frac{CO_2\ Captured^{Biomass}(t) \times Permanence(t) - CO_2\ Emitted^{Forestry\ Activities}(t)}{CO_2\ Captured^{Biomass}(t)} \quad (Eq.\ A.5)$$

$$Permanence(t) = (1 - RF(t)) \quad (Eq.\ A.6)$$

where:

- $CO_2\ Captured^{Biomass}(t)$ is the cumulative CO_2 captured via photosynthesis and sequestrated in biomass over time (t CO_2/ha);
- $CO_2\ Emitted^{Forestry\ Activities}(t)$ are the cumulative CO_2 emissions resulting from forestry activities over time (t CO_2/ha);
- $Permanence(t)$ is AR's permanence over time (%);
- $RF(t)$ is the risk of wildfires over time (See below) (%);
- and t is time (yrs).

In Section 2 of the main study (Value Chains of CDR Pathways), the Sankey diagrams (**Fig. 2**) represent AR's CDR efficiency in the UK over periods of 10, 30, 100 and 1,000 years, in order to account for the different and time-evolving contributions of the forest growth, the on-going maintenance of the forest, as well as the risk of wildfires over time.

Because temperate oceanic forests dominate the ecology of the UK—88% of the land cover in the UK— this ecological zone is used in this study as a proxy for the U [5]. Similarly, because conifers and broadleaves account for around half of the UK forest area—49% and 51% respectively[6], this distribution of tree species is used as a proxy for the UK as well.

SM.2.2. Risk of Wildfires/Permanence

Afforestation/reforestation is subject to disturbances—natural and unintended such as wildfires, insects or weather events, or anthropogenic and intended, such as harvest or deforestation—that decrease its CDR potential, and in fine CDR efficiency, over time. In particular, the penalty associated with the risk of wildfires RF can be quantified as a function of the wildfire's severity and frequency,

increasing over time. Adapted from (Hurteau et al., 2009)[10], the "fire-risk" model uses the following equation (**Eq. A.7**):

$$RF(t) = \begin{cases} 0, & t < mFRI \\ VDep \times \left(1 - \frac{mFRI}{t}\right), & t \geq mFRI \end{cases}$$

$(Eq\ A.7)$

where:

- $VDep$ is the vegetation departure index—ranging from 0% (zero potential biomass loss) to 100% (complete potential biomass loss) (%),
- $mFRI$ is the mean fire return interval—ranging from 0 years (very frequent) to 1,000 years (very rare) (yrs),

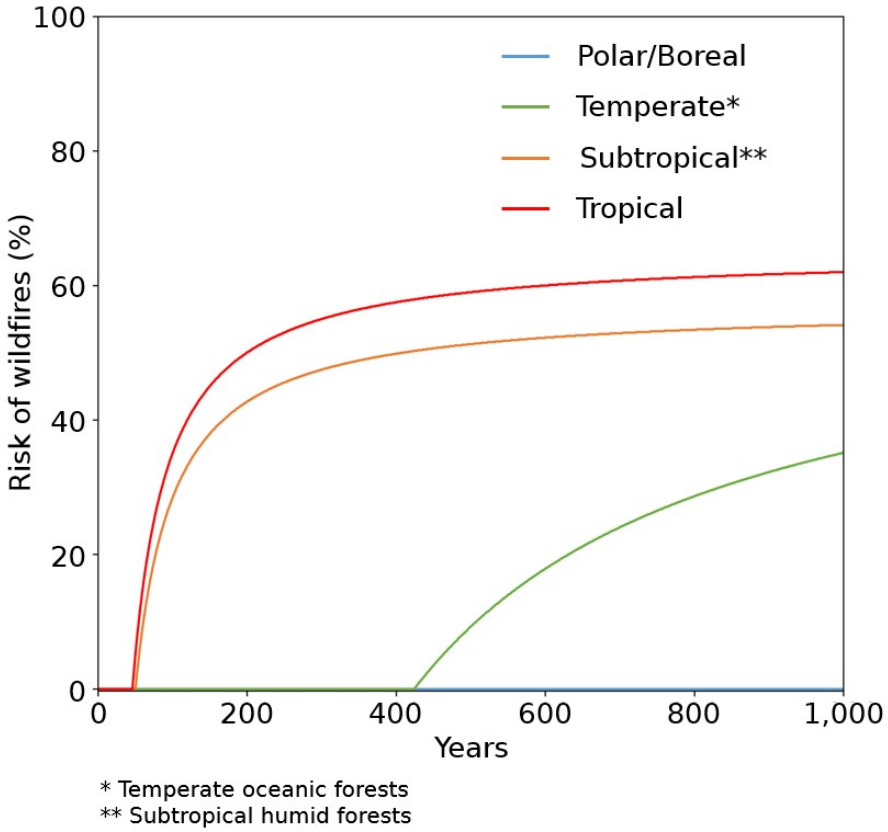

Fig. A.3 Evolution of the risk of wildfires over a period of 1,000 yrs for different climates.

- and t is the time (yrs).

Initially, VDep and mFRI are geo-spatial datasets from the LANDFIRE program [11] that cover the USA, but they have been processed—1) aggregated per ecological zones at the USA-scale [5], and 2) extrapolated to the word-scale—in the software ArcGIS. **Fig. A.3** shows the evolution of the risk of wildfires as a function of different climates over time. We observe that subtropical and tropical climates are the most affected by such risk, where it starts increasing after a period of 46-50 years (*i.e.,* mFRI in both climates, respectively), and up to 54-62% over 1,000 years. Specifically, the risk of

wildfires is greater in tropical climates than in subtropical climates, because the severity of wildfires, when occurring, is greater (*i.e.,* VDep of 65% and 57%, respectively). Conversely, the risk of wildfires is lower in temperate climates, both due to lower mFRI and VDep (*i.e.,* mFRI of 424 yrs and VDep of 61% in temperate oceanic forests), and almost inexistant in boreal climates (*i.e.,* mFRI of 1,000 yrs and VDep of 0%).

In Section 2 of the main study—in which the Sankey diagrams illustrate/represent the case of the UK, dominated by temperate climates—, the risk of wildfires is therefore null over 10, 30, and 100 years, but equal to 35% over a period of 1,000 years. In Section 3 of the main study (Timeliness & Permanence), different climates within different regions are represented in order to show the wide range of impact associated with the risk of wildfires, both in term of 1) when it starts increasing, and 2) how much it increases, on the CO_2 removal efficiency of AR.

SM.3. Bioenergy with CCS (BECCS)

This section presents the main assumptions that have been adopted for parameterizing BECCS in the MONET framework.

SM.3.1. Value Chain & Sankeys

Building on previous studies[12,13] BECCS's entire/full value chain is, here, explicitly spatio-temporally modelled, as shown **Fig. A.4**. This includes BECCS's biomass supply chain, *i.e.* LUC, biomass cultivation, processing and transport to the BECCS plant, biomass to energy conversion and CO_2 capture (at the BECCS plant), and CO_2 transport and storage. Different types of crops cultivated and/or collected different types of lands are analysed, as well as different biomass transport modes and distances (*i.e.,* local, imported biomass). Importantly, owing to the "carbon debt" initiated by land conversion to biomass production (which depends on the type of land that has been converted[14–16]), it usually takes some time for BECCS projects to bring net negative emissions. As a result, BECCS's CO_2 balance—the amount of CO2 captured minus the amount of CO2 emitted—, as well as BECCS's CDR efficiency are calculated cumulatively over time, in order to identify the time at which BECCS's "carbon debt" is paid off. This period of time is also referred as the carbon break-even time.

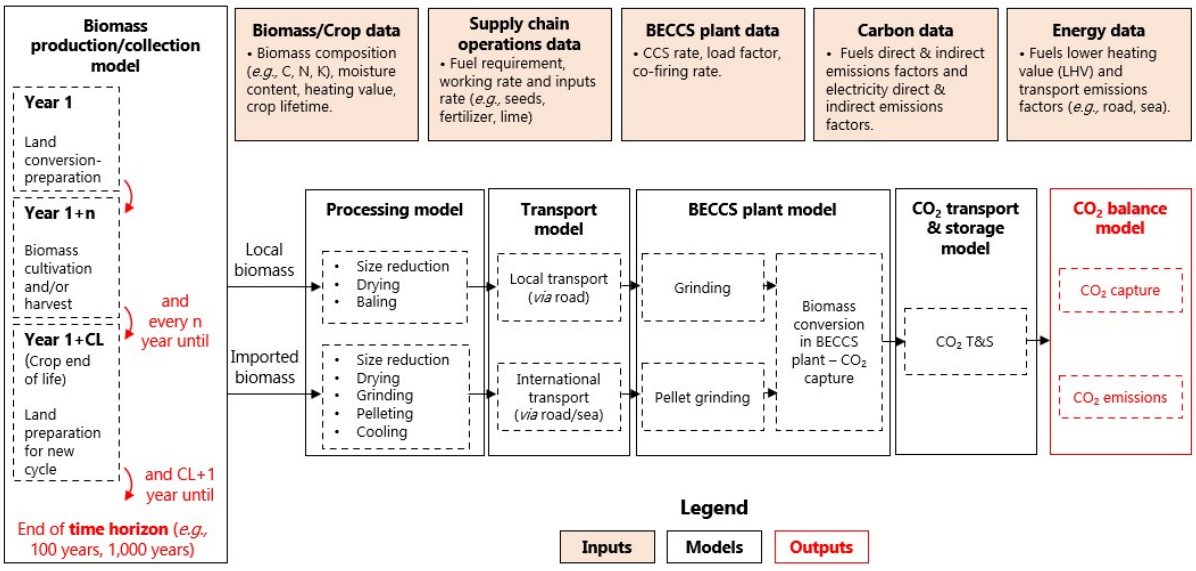

Fig. A.4 Schematic of the BECCS's whole-system model, outlining the interactions between each steps of biomass supply chain, BECCS power plant, and CO_2 transport & storage. Adapted from [12,13].

Overall, the CO_2 removal efficiency of BECCS $CO_2\,removal\,efficiency^{BECCS}(t)$ (%) is calculated as follows (**Eq. A.8-9**):

$$CO_2\,removal\,efficiency^{BECCS}(t) = \frac{\sum_t \left(CO_2\,Captured^{BECCS\,plant}(t) \times Permanence(t)\right) - \sum_t CO_2\,Emitted^{B}}{\sum_t CO_2\,Captured^{Biomass}(t)}$$

$$(Eq.\,A.8)$$

$$Permanence(t) = P_{geological\,reservoirs}(t)$$

$$(Eq.\,A.9)$$

where :

- $CO_2\,Captured^{BECCS\,plant}(t)$ is the annual amount of CO_2 captured at the BECCS plant over time (t CO_2/ha);
- $CO_2\,Emitted^{Biomass\,+\,CO_2\,SC}(t)$ is the annual amount of CO_2 emitted by the biomass supply chain and the T&S of CO_2 over time (t CO_2/ha);
- $(I)LUC$ is the initial "carbon dept" associated with direct and indirect land use change (t CO_2/ha);
- $Permanence(t)$ is BECCS's permanence over time (%). This is detailed below;
- and t is time (yrs).

In Section 2 of the main study, the Sankey diagrams (**Fig. 4**) represent BECCS's CDR efficiency in the UK over a period of 100. Different types of biomass cultivated on different types of land, and different transport modes and distance are illustrated, in order to account for a range of biomass cultivation and processing practices, as well as to evaluate the contribution of biomass transport and (I)LUC on BECCS's overall CO2 removal efficiency.

SM.3.2. Direct & Indirect Land Use Change ((I)LUC)/Permanence

When deploying BECCS, the conversion of the land on which the biomass is cultivated and/or harvested for BECCS results into land use change (LUC) and possibly indirect land use change (ILUC). (I)LUCs are associated with a CO_2 footprint, which takes more or less time to be compensated by BECCS's CO_2 removal potential. In other words, depending on the type of land on which the biomass used for BECCS, the CDR breakeven of BECCS—time at which BECCS has captured CO_2 than the CO_2 debt associated with (I)LUC, and therefore starts providing negative emissions.

For instance, converting an existing cropland into biomass cultivation for BECCS, results into 37,500 kgCO_2/ha of LUC[14] (due to the clearing of the land, and therefore the destruction of the natural CO_2 sink), but also 0.2 tCO_2/ha of ILUC[15,16], because the activity must be displaced and will itself create LUC somewhere else. **Table A.4** provide LUC and ILUC for different types of land. As a result with BECCS using indigenous energy-dedicated crop (Miscanthus) on cropland, BECCS's CDR breakeven time (CBT)

is 14 years. For forests and grasslands, it is 20 and 37 years respectively, whereas it is less than a year on MAL .

Table A.4 LUC and ILUC associated with different types of land, as well as BECCS's carbon break-even time (CBT), calculated in this study.

Land type	LUC (t CO_2/ha)	ILUC(t CO_2/ha)	References	BECCS's CBT (yrs)
Cropland	**38**	**183**	[14–16]	**14**
Grassland	**136**	**183**	[14–16]	**20**
Forest	**573**	**0**	[14,15]	**37**
MAL	**<1 (0.025)**	**0**	[14]	**<1**

SM.3.3. Permanence of geological reservoirs

For BECCS to generate negative emissions, the CO_2 captured by the BECCS plant is injected into geological reservoirs. Geological storage of CO_2 is a highly secure and therefore permanent climate change mitigation option. Based on Alcalde et al. (2018)[17], we assume that CO_2 leakage rate is as low as 0.0286% over 100 years, and remains below 0.532% over 10,000 years. This equates to simplified time-averaged linear leak rates of 0.0000532% per year, which we use to calculate the permanence of geological reservoirs through time, as follows:

$$P_{geological\ reservoirs}(t) = (1 - 0.0000532\%)^t$$

$$(Eq.\ A.10)$$

SM.4. Biochar

This section presents the main assumptions that have been adopted for parameterizing biochar in the MONET framework, and therefore in this study.

SM.4.1. Value Chain & Sankeys

Based on existing literature[18–22], biochar's entire/full value chain is explicitly spatio-temporally modelled, as shown **Fig. A.5** This includes the biomass supply chain, *i.e.* LUC, biomass cultivation, processing and transport to the pyrolysis plant, the pyrolysis plant and the biochar transport and application on soil. Different types of crops cultivated and/or collected different types of lands are analysed, as well as different pyrolysis processes (*i.e.,* slow, medium and fast pyrolysis). However, only the slow pyrolysis process is considered in this study, for reasons explained below.

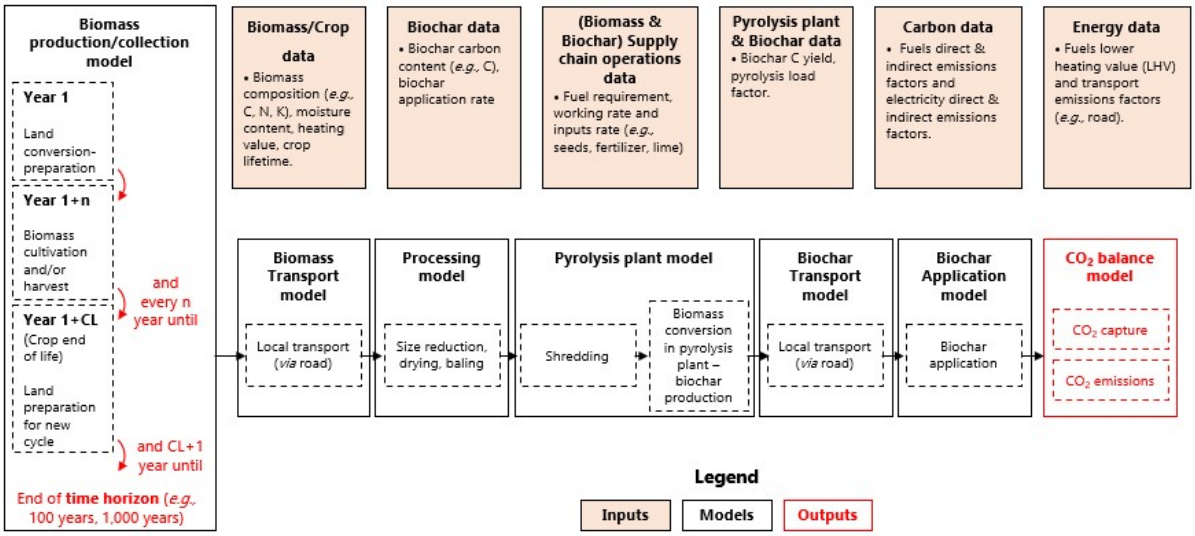

Fig. A.5 Schematic of the biochar's whole-system model, outlining the interactions between each steps of biomass supply chain, pyrolysis plant, and biochar supply chain.

Overall, the CO_2 removal efficiency of biochar $CO_2\ removal\ efficiency^{Biochar}(t)$ (%) is calculated as follows (**Eq. A.11-12**):

$$CO_2\ removal\ efficiency^{Biochar}(t) = \frac{\sum_t \left(CO_2\ Captured^{Pyrolysis\ plant}(t) \times Permanence(t)\right) - \sum_t CO_2\ Emitte}{\sum_t CO_2\ Captured^{Biomass}(t)}$$

$$(Eq\ A.11)$$

$$Permanence(t) = 1 - DC(t)$$

$$(Eq\ A.12)$$

where :

- $CO_2\ Captured^{Pyrolysis\ plant}(t)$ is the annual amount of CO_2 captured at the pyrolysis plant over time (t CO_2/ha);
- $CO_2\ Emitted^{Biomass\ +\ Biochar\ SC}(t)$ is the annual amount of CO_2 emitted by the biomass and biochar supply chains over time (t CO_2/ha);
- $(I)LUC$ is the initial "carbon dept" associated with direct and indirect land use change (t CO_2/ha);
- $Permanence(t)$ is biochar's permanence over time (%);
- $DC(t)$ is the decay rate of biochar over time (See below) (%);
- and t is time (yrs).

In Section 2 of the main study, the Sankey diagrams (**Fig. 6**) represent biochar's CDR efficiency in the UK over a period of 100. Different types of biomass cultivated on different types of land are illustrated,

in order to account for a range of biomass cultivation and processing practices, as well as to evaluate the contribution of (I)LUC on biochar's overall CO_2 removal efficiency.

SM.4.2. Decay Rate/Permanence

Biochar is a carbon rich material, comprised of both aliphatic and aromatic compounds, having different rate of persistence in soil. The latter can be expressed as a two-pool exponential decay rate (DR) [18,22,23]—the labile (*i.e.,* rapid decay) and recalcitrant (*i.e.,* slow decay) pools—as follows (**Eq. A.13**):

$$DR(t) = L \times exp\left(\frac{-ln(2)}{t_{1/2L}} \times t\right) + R \times exp\left(\frac{-ln(2)}{t_{1/2R}} \times t\right) \quad (Eq\ A.13)$$

where:

L is the labile fraction of biochar (%);

R is the recalcitrant fraction of biochar (%) — with $L + R = 1$;

$t_{1/2L}$ is the labile half-time (yrs);

$t_{1/2R}$ is the recalcitrant half-time (yrs);

and t is the time (yrs).

Biochar's decay rate is function of the biochar properties, *i.e.* how recalcitrant the carbon compounds in the biochar are to biotic and abiotic degradation). Generally expressed as the molar ratio of hydrogen to organic carbon H/C_{org}, biochar properties depend on the pyrolysis temperature (*i.e.,* slow or fast pyrolysis) and the biomass feedstock used to produce biochar[22–24].

As shown in **Fig. A.6**, the estimated persistence of biochar is lower for slow pyrolysis processes than for fast ones (*i.e.,* lower pyrolysis temperatures). In addition, biochar's decay rate is also a function of the soil characteristics, on which it is applied. In particular, higher soil temperatures reduce biochar's persistence, mainly due to the enhanced intensity of biotic and/or abiotic processes, *e.g.* increased microbial activity, sorption, desorption, and/or organo-mineral interactions[22,25]. As a result, the estimated longevity of biochar accumulated in soil decrases more rapidly in tropical climates (*e.g.,* in Brazil, where the surface soil temperature is usally around 30C) than in temperate ones (*e.g.* in the UK), especially if slower pyrolysis processes have been adopted. Key scenarios inputs for **Fig. A.6** are summarised in **Table A.5**.

Table A.5 Two-pool exponential model for biochar's decay rate, under different scenarios (i.e., pyrolysis temperature and soil temperature).

Scenario	Pyrolysis temperature (°C)	Soil temperature (°C)	L[a] (%)	R[a] (%)	$t_{1/2L}$[a] (years)	$t_{1/2R}$[a] (years)	Decay rate[b] (%)		
							Over 100 yrs	Over 500 yrs	Over 1,000 yrs
Slow pyrolysis - UK	350–450°C	10.9	46	54	104	460	70	27	12
Slow pyrolysis - Brazil	350–450°C	25	77	23	84	515	54	13	6
Medium	450–600°C	10.9	29	71	92	617	64	41	23

pyrolysis - UK									
Fast pyrolysis - UK	≥ 600°C	10.9	40	60	270	1075	87	54	34
Fast pyrolysis - Brazil	≥ 600°C	25	44	56	136	575	76	34	17

[a] Data interpolated from (Woolf et al., 2021)[22].
[b] Data from (Woolf et al., 2021)[22].

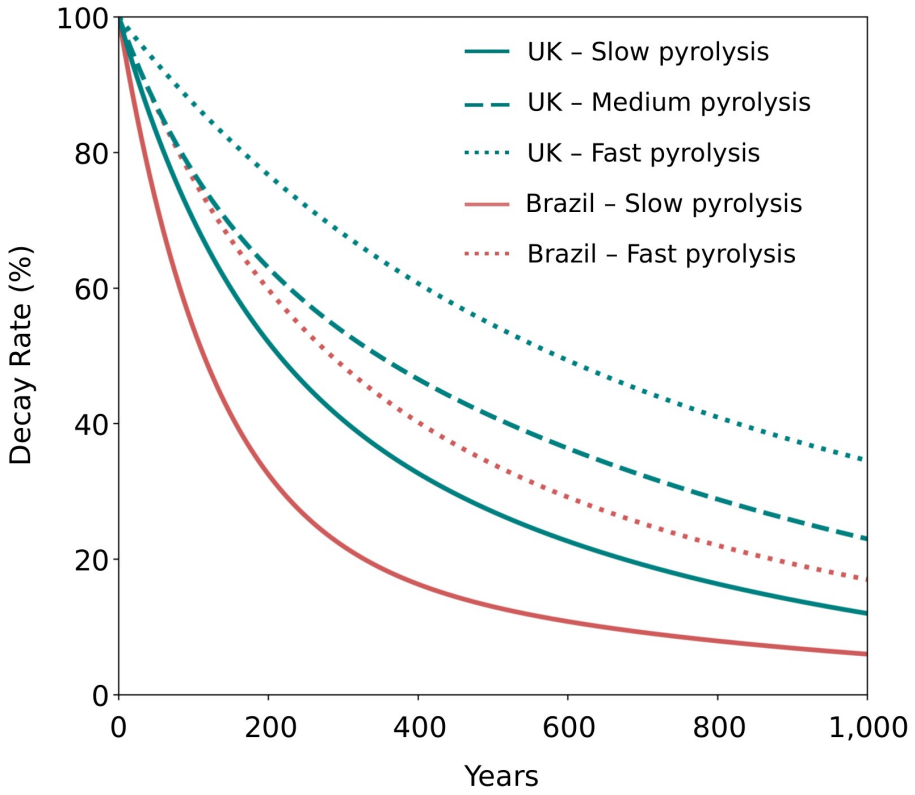

Fig. A.6 Different decay rates for biochar over 1,000 years.

Finally, although fast pyrolysis processes result into more persistent biochar (and therefore more permanent CDR), the share of biochar produced is lower than in the case of slow pyrolysis processes—biochar yield decreases from 40% (*i.e.,* C yield of 48-61%) to 12% (*i.e.,* C yield of 14-18% C) — and are therefore, overall, less efficient, as shown in **Fig. A.7**. For this reason, if biochar is produced for the purpose of achieving CDR, then only slow pyrolysis processes should be considered.

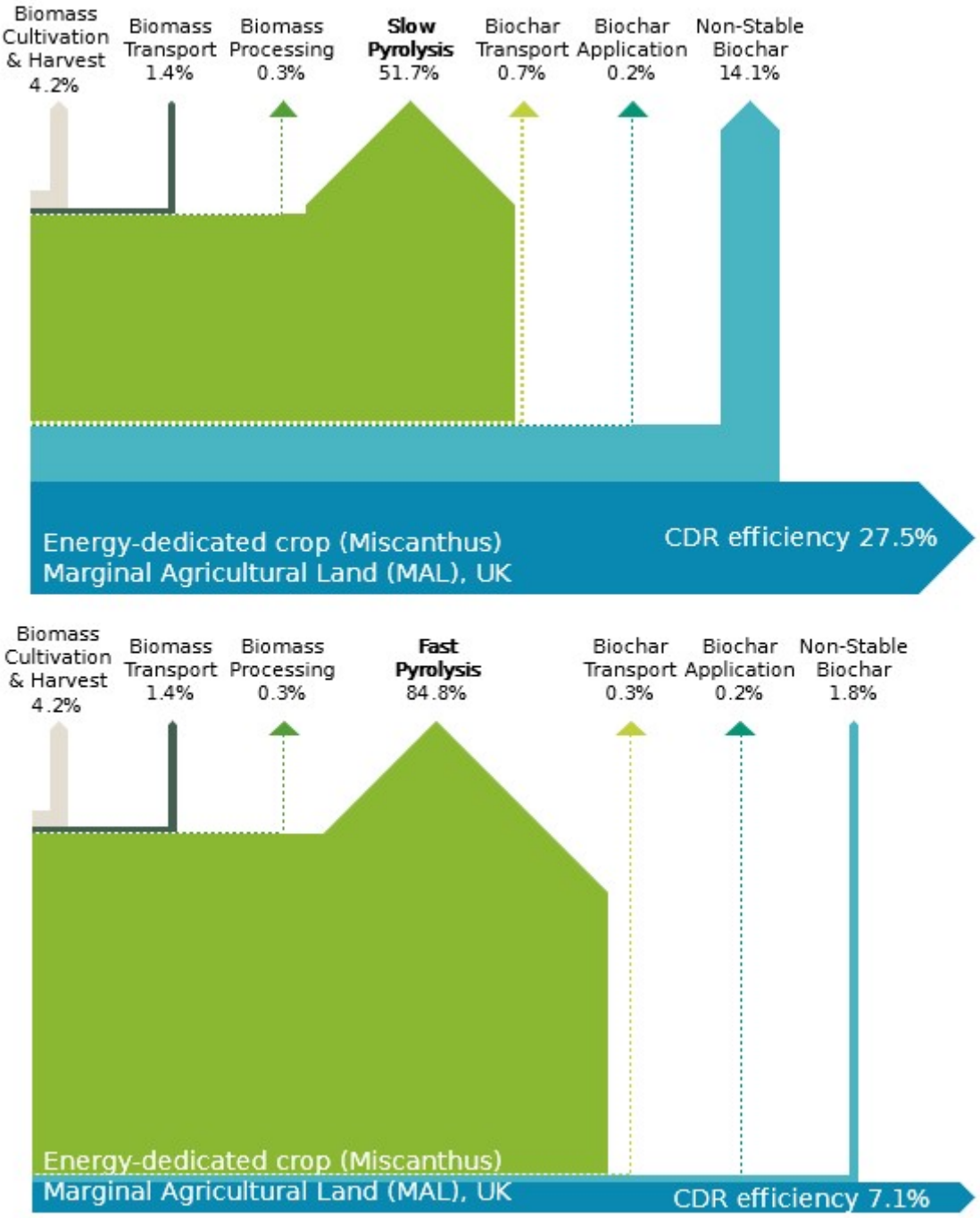

Fig. A.7 Comparison of CDR efficiencies between slow-pyrolysis and fast-pyrolysis.

SM.5. Direct Air Capture with CCS (DACCS)

This section presents the main assumptions that have been adopted for parameterizing DACCS in the MONET framework, and therefore in this study.

SM.5.1. Value Chain & Sankeys

Three DACCS technologies are considered in this study, for which their entire value chains are explicitly spatio-temporally modelled, as shown **Fig. A.8** : A solid sorbent DAC technology and a liquid solvent for the capture of CO_2 directly from the air[26] and sea water mineralisation for the capture of CO_2 from the sea[27]. For the liquid solvent DACCS, high-grade heat (*i.e.,* 900°C[2,3]) is either provided by natural

gas or by hydrogen and power by the electricity grid in the UK. In particular, based on (Keith et al., 2018)[3], the CO_2 emissions resulting from the combustion of natural gas are captured within the DAC plant. For the solid sorbent DACCS, heat and power are provided by the electricity grid in the UK, and we assume the use of a heat pump (COP = 3) for the conversion of the grid power to low-grade heat (*i.e.,* ~100°C[2]).

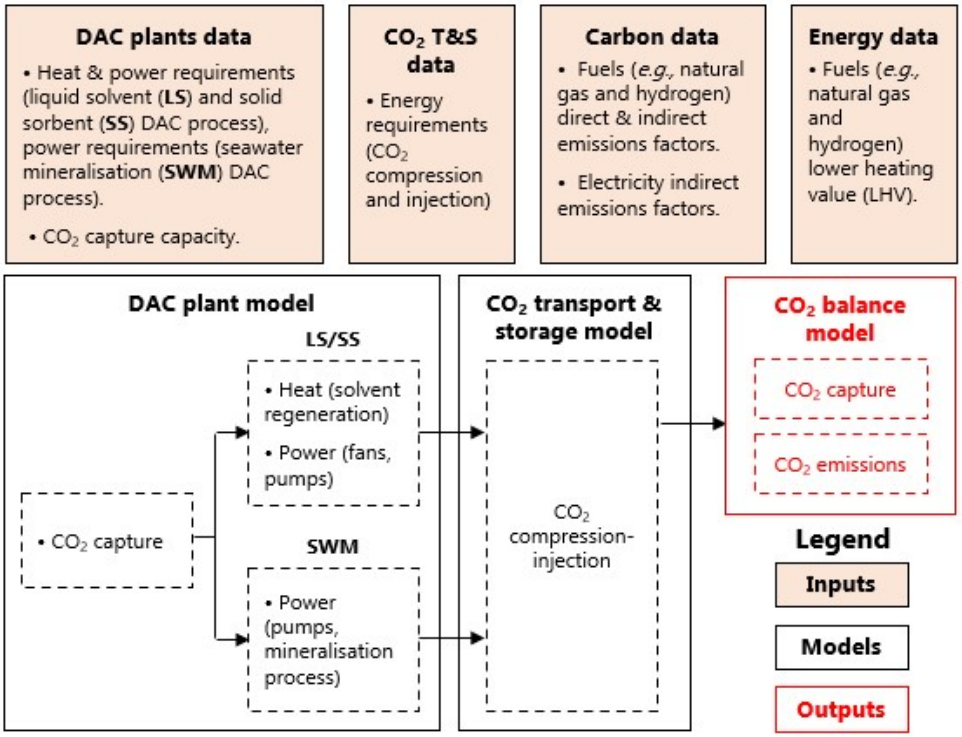

Fig. A.8 Schematic of the DACCS's whole-system model, for the liquid solvent (LS), solid sorbent (SS), and seawater mineralisation (SWM) DAC technologies.

SM.5.2. Decarbonisation of the Energy Sector

DACCS's CDR efficiency is mainly reduced by the carbon intensity of the energy used, which vary with the DAC technology (*i.e.,* solid sorbent, liquid solvent or seawater mineralisation), with the region in which, and when, it is deployed. The decarbonisation of energy sector, in particular the heat supply (*via* natural gas, hydrogen or electricity) and the electricity grid, is detailed in Section A.1.

SM.5.3. Permanence of geological reservoirs

See Section A.3.3.

SM.6. Enhanced Weathering (EW)

SM.6.1. Value Chain & Sankeys

Based on existing literature[28–31], EW's entire/full value chain is explicitly spatio-temporally modelled, as shown **Fig. A.9**.

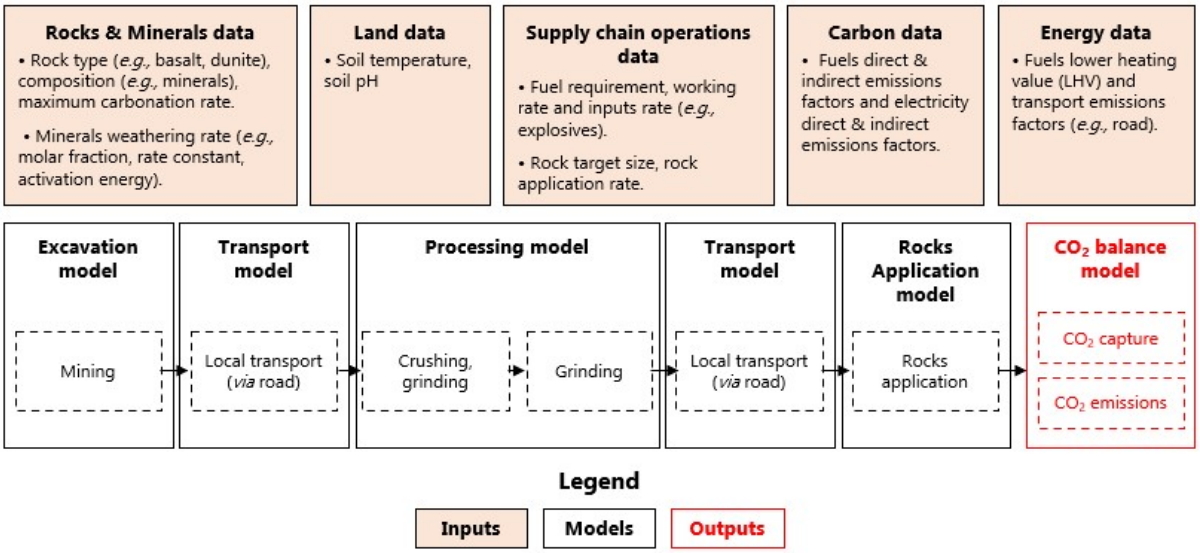

Fig. A.9 Schematic of the EW's whole-system model, outlining each steps of the rocks supply chain.

SM.6.2. CO_2 sequestration Potential & Carbonation Rate

Enhanced weathering's CO_2 sequestration potential increases over time, as silicate rocks weather, and saturates (permanently) afterwards, once the rocks are fully weathered. By then, the rocks have reached their maximum CO_2 sequestration potential, which is inherently permanent.

As detailed in (Beerling et al., 2020)[32], the chemical reactions involved with the rocks weathering process are 1) the formation of ions HCO_3^-, resulting from the transfer of base cations, such as calcium ions (Ca^{2+}), from soil drainage waters to surface waters, and then 2) the precipitation of calcium carbonate ($CaCO_3$), resulting from the transport of ions Ca^{2+} and HCO_3^- to the ocean. These two reactions are shown below (**Eq. A.14-15**):

The chemical reactions involved with the rocks weathering process are 1) the formation of bicarbonate ions (HCO_3^-), resulting from the transfer of base cations, such as calcium (Ca^{2+}) or magnesium (Mg^{2+}) ions, from soil drainage waters to surface waters (when the rocks are exposed to water) (**Eq. A.14-15**), and 2) the precipitation of calcium carbonate ($CaCO_3$), resulting from the transport of ions HCO_3^- to the ocean, and their reactions with ions Ca^{2+} (**Eq. A.16**).

For example, forsterite (silicate mineral) is dissolved trough the following reaction:

$$CaSiO_3 + 2CO_2 + 3H_2O \rightarrow Ca^{2+} + 2HCO_3^- + H4SiO_4$$

$(Eq\ A.14)$

Wollastonite (another silicate mineral) is, instead, dissolved through the following reaction:

$$Mg_2SiO_4 + 4CO_2 + 4H_2O \rightarrow 2Mg^{2+} + 4HCO_3^- + H4SiO_4$$

$(Eq\ A.15)$

Eventually, part of the ions HCO_3^- are transported to the ocean, where they are mineralised following the reaction below:

$$Ca^{2+} + 2HCO_3^- \rightarrow CaCO_3 + CO_2 + H_2O$$

$(Eq\ A.16)$

Whilst in the first two reactions (**Eq. A.14-15**), 2 moles of CO_2 are sequestrated for 1 mole of Ca^{2+} or Mg^{2+}, 1 mol of CO_2 is emitted back, into the ocean, in the third reaction (**Eq. A.16**).
Overall, because not all bicarbonate ions (resulting from **Eq. A.14-15**) are transported to the ocean and then mineralised, it is conventionally assumed that, overall, 1.7 mol of CO_2 is sequestrated per mol divalent cation produced[28,29,32]—the CO_2 sequestration potential of a rock is equal to 1.7 times its carbonation potential.

As such, EW's CO_2 sequestration potential $CO_2\ sequestration\ potential^{\ EW}(t)$ over time (t CO_2/t rock) is evaluated as follows:

$$CO_2\ sequestration\ potential^{\ EW}(t) = \omega\ \times Carbonation\ potential^{\ EW}\ \times CR(t)$$
$$(Eq\ A.17)$$

where:

- $Carbonation\ potential^{\ EW}$ is the maximum/theoretical carbonation potential of silicate rocks (t CO_2/t rock);
- ω is the "carbonation to CO_2 sequestration" conversion factor (%), which accounts for the additional drawdown from cation flux into the ocean. As explained above, $\omega = 1.7$;
- $CR(t)$ is the carbonation rate of EW over time (%);
- and t is time (yrs).

Typically, carbonation rate CR—the share of rock that weathers every year—is a function of the rock weathering rate WR—itself function of soil characteristics, *i.e.* temperature[33] and pH[34], and mineral composition—and size of rock [29,35]. WR can be modelled as a function of the soil pH pH and temperature T and the mineral composition m, using generalized equations for the linear transition state theory law, as in (Beerling et al, 2020)[36] and (Tayor et al, 2016)[37] and CR can then be modelled with a shrinking core model, as suggested in (Renforth, 2012)[28] . This is shown in the following equations (**Eq. A.18-20**).

The carbonation rate CR is expressed as follows:

$$CR(t,d_T) = \frac{d_T^3 - \left(d_T - 2 \times WR \times V_m t\right)^3}{d_T^3}$$
$$(Eq\ A.18)$$

where:

- d_T is the target rock size after grinding (m),
- WR is the weathering rate of the rock (mol m^{-2} s^{-1}),
- V_m is the molar volume of the rock (m^3 mol^{-1}),
- and t is the time (s).

The weathering rate WR is expressed as follows:

$$WR = \frac{\sum_m Mf_m \times Mm_m \times WR_m}{\sum_m Mf_m \times Mm_m}$$

$(Eq\ A.19)$

where:

- Mf_m is the molar fraction of the mineral m within the rock (‰),
- Mm_m is the molar mass/weight of the mineral m within the rock (g mol^{-1}),
- and WR_m is the weathering rate of the mineral m (mol m^{-2} s^{-1}).

And the weathering rate of a mineral m WR_m applied to a soil with pH pH and temperature T is expressed as follows:

$$WR_m(pH,T) = k_{H^+} \times e^{-\frac{Ea_{H^+}}{R} \times \left(\frac{1}{T} - \frac{1}{298.15}\right)} \times 10^{-n_{H^+} \times pH} + k_{H_2O} \times e^{-\frac{Ea_{H_2O}}{R} \times \left(\frac{1}{T} - \frac{1}{29}\right.} \times e^{-\frac{Ea_{HO^-}}{R} \times \left(\frac{1}{T} - \frac{1}{298.15}\right)} \times 10^{n_{HO^-} \times (pH - 14)}$$

$(Eq\ A.20)$

where:

- k_i is the rate constant of the individual weathering agent, *e.g.* [H^+], [H_2O] or [HO^-] (mol m^{-2} s^{-1}),
- Ea_i is the apparent activation energy of the individual weathering agent (kJ mol^{-1}),
- R is the gas constant (kJ mol^{-1} K^{-1}),
- and n_i is the reaction order of the individual weathering agent (-).

As shown in **Fig. A.10,** EW's carbonation rate is a function of the rocks properties (*i.e.,* type, composition and size). For example, the carbonation rate of rocks increases as the size of the rocks decreases—it takes about 250 years for 10 µm fast-weathering basalts to be entirely weathered, whereas it takes more than a millennium for 50 µm ones. Another example shows that, owing to the type and composition of the rocks, dunite rocks weather faster than fast-weathering basalt, themselves faster than slow-weathering basalts—it takes respectively 35, 250, and 580 years for these rocks, all ground to 10 µm and applied in the UK, to reach their maximum carbonation potential.
Moreover, EW's carbonation rate is also a function of the soil on which the rocks are applied (*i.e.,* soil temperature and pH). For example, increasing soil temperatures result into higher weathering rates, and therefore faster carbonation rates—it only takes 113 years in Brazil (where the average soil temperature is about 30), compared to 250 years in the UK (where it is about 10.8), for 10 µm fast-weathering basalts to be entirely weathered. A last example shows that extreme pH values (towards acid or base) also result into faster carbonation rates—it takes 375 years in China (where the average soil pH is about 7), compared to only 250 years in the UK (where it is about 5.4), for 10 µm fast-weathering basalts to be entirely weathered.

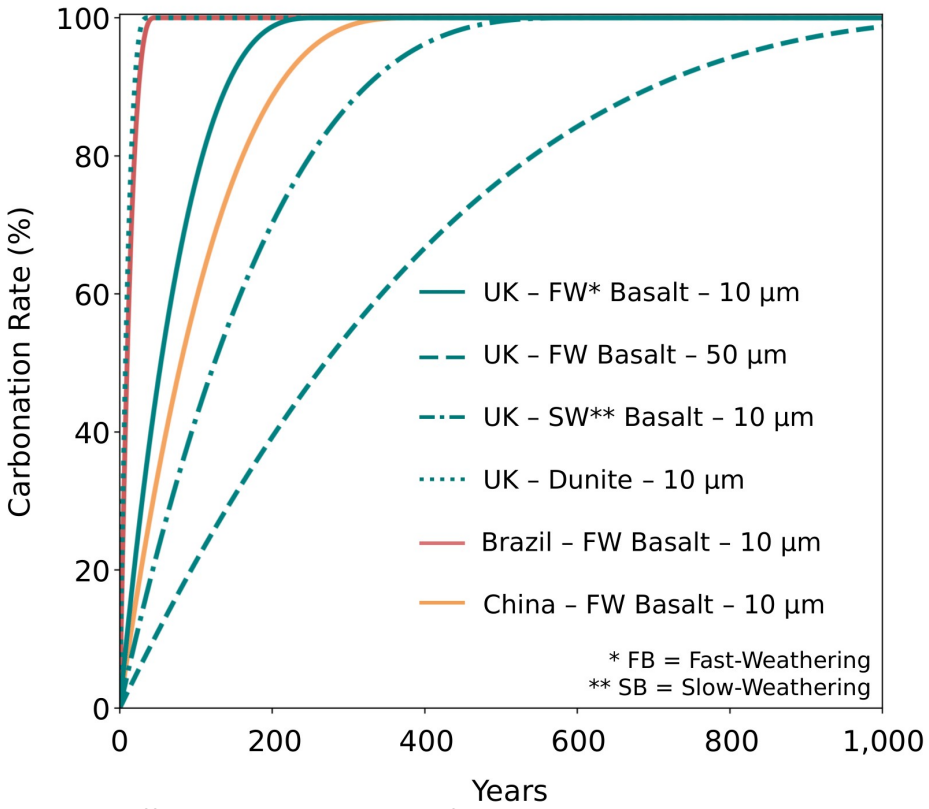

Fig. A.10 Different carbonation rates for EW over 1,000 years.

Finally, we recognise that when rocks are ground to a specific size target, the resulting size of grinded rocks usually follows a distribution[28,32], rather than a single rock size. The resulting carbonation rate CR_{dist} is therefore equal to the weighted sum of the $CR^{(d_T)}$, specific to a size d_T, as shown below:

$$CR_{dist}(t) = \sum_{d_T} CR(t,d_T)$$

$$(Eq\ A.21)$$

However, this is not accounted for in this work, we only assess CR for a single target rock size—either 10 or 50 µm—as the aim is to emphasize and provide insights on the key elements that impact EW's CDR efficiency the most.

References

1 D. Huppmann, E. Kriegler, V. Krey, K. Riahi, J. Rogelj, S. K. Rose, J. Weyant, N. Bauer, C. Bertram, V. Bosetti, K. Calvin, J. Doelman, L. Drouet, J. Emmerling, S. Frank, S. Fujim and R. Zhang., *Integr. Assess. Model. Consort. Int. Inst. Appl. Syst. Anal.*, 2018, DOI:10.22022/SR15/08-2018.15429.

2 M. Fasihi, O. Efimova and C. Breyer, *J. Clean. Prod.*, 2019, **224**, 957–980.

3 D. W. Keith, G. Holmes, D. St. Angelo and K. Heidel, *Joule*, 2018, **2**, 1573–1594.

4 N. Mac Dowell and M. Bui, Eds., *Greenhouse Gas Removal Technologies*, Royal Society of Chemistry, 2022.

5 FAO, *Global Ecological Zones for FAO Forest Reporting: 2010 Update*, Rome, 2011.

6 FOREST EUROPE, *State of Europe's Forests 2020*, 2020.

7 C. Whittaker, N. Mortimer, R. Murphy and R. Matthews, *Biomass and Bioenergy*, 2011, **35**, 4581–4594.

8 J. Morison, R. Matthews, G. Miller, M. Perks, T. Randle, E. Vanguelova, M. White and S. Yamulki, *Understanding the carbon and greenhouse gas balance of forests in Britain*, 2012.

9 M. Röder, C. Whittaker and P. Thornley, *Biomass and Bioenergy*, 2015, **79**, 50–63.

10 M. D. Hurteau, B. A. Hungate and G. W. Koch, *Carbon Balance Manag.*, 2009, **4**, 1.

11 LANDFIRE Program: Home, https://www.landfire.gov/index.php, (accessed 17 January 2021).

12 M. Fajardy and N. Mac Dowell, *Energy Environ. Sci.*, 2017, **10**, 1389–1426.

13 M. Fajardy, Imperial College London, 2020.

14 J. Fargione, J. Hill, D. Tilman, S. Polasky and P. Hawthorne, *Science*, 2008, **319**, 1235–1238.

15 R. J. Plevin, M. O'Hare, A. D. Jones, M. S. Torn and H. K. Gibbs, *Environ. Sci. Technol.*, 2010, **44**, 8015–8021.

16 K. P. Overmars, E. Stehfest, J. P. M. Ros and A. G. Prins, *Environ. Sci. Policy*, 2011, **14**, 248–257.

17 J. Alcalde, S. Flude, M. Wilkinson, G. Johnson, K. Edlmann, C. E. Bond, V. Scott, S. M. V. Gilfillan, X. Ogaya and R. S. Haszeldine, *Nat. Commun.*, 2018, **9**, 2201.

18 D. Woolf, J. E. Amonette, F. A. Street-Perrott, J. Lehmann and S. Joseph, *Nat. Commun.*, 2010, DOI:10.1038/ncomms1053.

19 K. G. Roberts, B. A. Gloy, S. Joseph, N. R. Scott and J. Lehmann, *Environ. Sci. Technol.*, 2010, **44**, 827–833.

20 S. Shackley, J. Hammond, J. Gaunt and R. Ibarrola, *Carbon Manag.*, 2011, **2**, 335–356.

21 J. L. Gaunt and J. Lehmann, *Environ. Sci. Technol.*, 2008, **42**, 4152–4158.

22 D. Woolf, J. Lehmann, S. Ogle, A. W. Kishimoto-Mo, B. McConkey and J. Baldock, *Environ. Sci. Technol.*, 2021, **55**, 14795–14805.

23 S. Bakshi, C. Banik and D. A. Laird, *Sci. Rep.*, 2020, **10**, 13082.

24 J. Wang, Z. Xiong and Y. Kuzyakov, *GCB Bioenergy*, 2016, **8**, 512–523.

25 Y. Fang, B. Singh and B. P. Singh, *Soil Biol. Biochem.*, 2015, **80**, 136–145.

26 National Academies of Sciences, *Negative Emissions Technologies and Reliable Sequestration: A Research Agenda*, 2019.

27 E. C. La Plante, D. A. Simonetti, J. Wang, A. Al-Turki, X. Chen, D. Jassby and G. N. Sant, *ACS Sustain. Chem. Eng.*, 2021, **9**, 1073–1089.

28 P. Renforth, *Int. J. Greenh. Gas Control*, 2012, **10**, 229–243.

29 J. Strefler, T. Amann, N. Bauer, E. Kriegler and J. Hartmann, *Environ. Res. Lett.*, 2018, **13**,

034010.

30 D. Lefebvre, P. Goglio, A. Williams, D. A. C. Manning, A. C. de Azevedo, M. Bergmann, J. Meersmans and P. Smith, *J. Clean. Prod.*, 2019, **233**, 468–481.

31 N. Moosdorf, P. Renforth and J. Hartmann, *Environ. Sci. Technol.*, 2014, **48**, 4809–4816.

32 D. J. Beerling, E. P. Kantzas, M. R. Lomas, P. Wade, R. M. Eufrasio, P. Renforth, B. Sarkar, M. G. Andrews, R. H. James, C. R. Pearce, J. F. Mercure, H. Pollitt, P. B. Holden, N. R. Edwards, M. Khanna, L. Koh, S. Quegan, N. F. Pidgeon, I. A. Janssens, J. Hansen and S. A. Banwart, *Nature*, 2020, **583**, 242–248.

33 Z. Wan, S. Hook and G. Hulley, MOD11C3 MODIS/Terra Land Surface Temperature/Emissivity Monthly L3 Global 0.05Deg CMG V006 (accessed 17 January 2021).

34 W. R. Wieder, J. Boehnert, G. B. Bonan and M. Langseth, 2014.

35 T. Rinder and C. von Hagke, *J. Clean. Prod.*, 2021, **315**, 128178.

36 D. J. Beerling, E. P. Kantzas, M. R. Lomas, P. Wade, R. M. Eufrasio, P. Renforth, B. Sarkar, M. G. Andrews, R. H. James, C. R. Pearce, J. F. Mercure, H. Pollitt, P. B. Holden, N. R. Edwards, M. Khanna, L. Koh, S. Quegan, N. F. Pidgeon, I. A. Janssens, J. Hansen and S. A. Banwart, *Nature*, 2020, **583**, 242–248.

37 L. L. Taylor, J. Quirk, R. M. S. Thorley, P. A. Kharecha, J. Hansen, A. Ridgwell, M. R. Lomas, S. A. Banwart and D. J. Beerling, *Nat. Clim. Chang.*, 2016, **6**, 402–406.